Heterogeneous drying and nonmonotonic contact angle dynamics in concentrated film-forming latex drops

Subhalakshmi Kumar
Department of Chemical and Biomolecular Engineering, University of Illinois at Urbana-Champaign, Urbana, Illinois 61801, USA

Joshua S. Katz
Formulation Science, Core R&D, The Dow Chemical Company, Collegeville, Pennsylvania 19426, USA

Charles M. Schroeder*
Department of Chemical and Biomolecular Engineering, Department of Materials Science and Engineering, University of Illinois at Urbana-Champaign, Urbana, Illinois 61801, USA
(Received 2 March 2017; published 22 November 2017)

The dynamic drying process is studied in spatially heterogeneous film-forming latex suspensions across a wide range of dispersion concentrations using optical imaging techniques. Systematic changes in latex suspension concentration are found to affect lateral drying heterogeneity and surface topology. A nonmonotonic decay in contact angle is observed at the edges of drying droplets by continuously monitoring evaporation dynamics, which is quantitatively characterized by the peak strain and peak formation time. An analytical model is developed to explain the nonmonotonic contact-angle decay by considering a transient dilational stress imposed on a viscoelastic solid model for the particle network. Importantly, the latex concentration dependence of this phenomenon provides evidence for a smooth transition from fluid-line pinning to fluid-line recession behavior during drying, leading to ringlike to volcanolike deposition patterns, respectively. Using experimental data for drying heterogeneity, we quantitatively explore the influence of Marangoni flow and capillary pressure on drying behavior. Moreover, our results show that latex concentration and particle packing can also be strategically used to reduce contact-line friction, thereby affecting fluid-line recession. Taken together, these results show that studying latex suspensions in seemingly simple droplet geometries provides insight into the emergent spatially heterogeneous viscoelastic properties during film formation.

DOI: 10.1103/PhysRevFluids.2.114304

I. INTRODUCTION

Film-forming latex suspensions have long served as a robust and popular industrial coating material. Common applications include latex-based inks, paints, and coatings for adhesives, sealants, and pressure-sensitive materials [1,2]. For these applications, the formulation composition (e.g., latexes, binders, pigments, and additives) and corresponding flow properties of these materials are remarkably diverse. Latex particles are the primary film-forming component in latex-based suspensions, generally comprising 20%–40% of the dispersion weight, in addition to additives such as surfactants and stabilizers. The drying process is directly impacted by the physical properties of film-forming suspensions, including surface tension at the liquid-air interface [3], the identity of the solid-liquid interface [4], the fluid mechanics of the suspension [5], contact-line dynamics [4,6], and dynamically emerging deposition patterns [7,8]. However, most of these properties depend on latex and surfactant concentration, which in turn complicates a quantitative understanding of system dynamics.

*cms@illinois.edu

Despite widespread implementation, the drying behavior of film-forming latex suspensions is not fully understood. Rapid evaporation in water-based formulations can lead to undesirably short open times, defined as the longest time after initial deposition at which additional layers can be seamlessly merged for structural, optical, and functional continuity. Moreover, spatially nonuniform drying can result in unwanted heterogeneities in coatings. For example, rapid fluid-line recession can result in relatively fast drying at the edges of a coating compared to the center portions of a drop or film (known as lateral drying heterogeneity), which is known to drastically reduce open time [2]. The rate of fluid-line recession is also known to affect surface deposition topologies in drying films, which can lead to inhomogeneities and inefficient interlayer stacking [9–14]. Spatially inhomogeneous drying can also occur at the top interface of a coating (known as vertical drying heterogeneity), which can lead to compromised structural integrity and films with reduced mechanical strength. From this perspective, there is a strong need to understand the fundamental phenomena that govern the drying heterogeneity processes in these materials.

In recent years, sessile drop-drying experiments [5,15] have been used to study emergent deposition behaviors such as the coffee-ring effect [15] and the role of surface tension and Marangoni flow in determining deposition patterns [16]. Evaporation of droplets laden with colloidal particles has been studied numerically in the limit of rapid evaporation [17] and drying droplets of colloidal suspensions on rough surfaces were recently studied using simulations [18]. However, most prior studies have focused on dispersions in the dilute or ultradilute concentration regime, which are known to exhibit qualitatively different drying dynamics compared to more concentrated suspensions [8,19]. A schematic of the drop-drying process for the ultradilute and concentrated regimes is shown in Fig. 1. In the ultradilute case, drops dry with either a pinned contact line (with decreasing contact angle) or a receding contact line (with fixed contact angle). On the other hand, concentrated film-forming suspensions generally cannot be analyzed using this simplistic framework. The ideal film-forming process is known to occur in three stages [1,2]: (1) particle packing and emergence of local structure due to evaporation, (2) particle deformation due to interactions with neighboring particles, and (3) particle coalescence and the formation of a continuous polymer film. During stage 1, evaporation leads to an increase in salt concentration, thereby causing a dramatic decrease in the Debye length and screening of charge repulsion, enabling close packing of particles. The interparticle voids in the close-packed structure disappear in stage 2, which brings neighboring particle interfaces in close range for van der Waals forces [2] to become dominant. During the final stage, interdiffusion of chains across individual particle interfaces leads to a homogeneous film.

In droplets of concentrated latex suspensions, heterogeneity in particle concentration and topology rapidly emerges during the drying process as particles partition at the edges and form densely packed regions while the drop center has particle-deficient fluidic regions (Fig. 1, bottom). Regions within the same drop include a dry region beyond the fluid line with particles in random close packing, a drying front of close-packed particles saturated with water located at the receding fluid line, a packing front of concentrated particles with volume fraction below close packing, and the fluidic region near the drop center. In this way, gradients in latex particulate concentration can give rise to complex phenomena due to rheological heterogeneities and material property differences in adjacent regions. In particular, fluid-line recession occurs when the pressure drop required to sustain fluid flow through the densely packed bed towards the outer portions of the droplet exceeds the capillary pressure at the edges [12]. Interfacial concentration gradients give rise to an additional flow, known as Marangoni flow, that drives material toward the drop center [2], especially for surfactant-coated or charge-stabilized particles. An additional complexity in film-forming latexes lies in the dynamic changes in surface properties during drying. Unlike stabilized colloidal suspensions where the identity of individual particles is preserved after drying, a hydrophobic polymer film is left behind after drying in film-forming latexes. The influence of time-dependent changes in surface properties on the dynamics of fluid-line recession (and ultimately deposition topology) is not fully understood. One could hypothesize that the aqueous fluid line is able to rapidly recede, whereas the nascent polymer film at the initial contact line remains effectively pinned during drying. However, the degree of hydrophobicity within the dry region critically depends on the extent of evaporation from

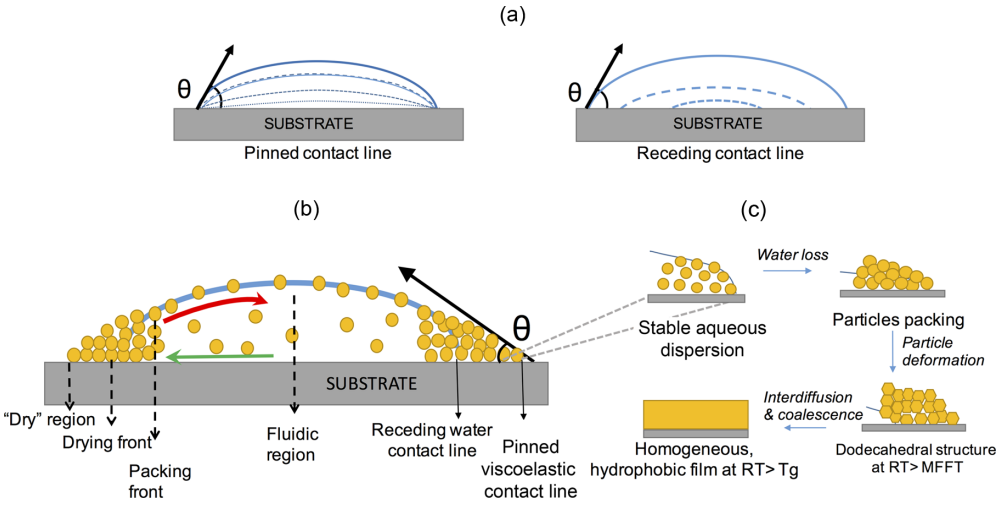

FIG. 1. Drying mechanisms in dilute, concentrated, and film-forming suspensions. (a) Dilute dispersion: drying in ultradilute suspensions showing a pinned contact line (left) and receding contact line (right). Time progression is denoted by dotted lines. The contact angle either decreases monotonically for the first case or remains constant at equilibrium values in the latter case. (b) Concentrated film-forming dispersion: emergent heterogeneity in concentrated latex suspensions. A radially outward capillary flow (green arrow) causes particles to partition preferentially at the drop edge. This leads to two effects: First, an interfacial gradient in surface active agents causes a counter Marangoni flow (red arrow) and second, a reduction of pressure at the drop edge due to particle close packing leads to fluid-line recession. Regions within the same drop include a dry region beyond the fluid line with particles in random close packing, a drying front of close-packed particles saturated with water at the receding fluid line, a packing front of concentrated particles with volume fraction below close packing, and the fluidic center. (c) Stages of film formation. Latex particles in an initially stable aqueous dispersion closely pack at the drop edge, which increases resistance to fluid flow in the particle interstices and causes the fluid line to recede. As evaporation continues, interparticle voids are lost and particles deform from their spherical shape while initially maintaining their individual particle identities. Continued evaporation causes the particle layer to turn transparent due to homogenization of the refractive index, which often signals film formation. Further macromolecular interdiffusion and coalescence between boundaries at $T > T_g$ causes formation of a homogeneous, continuous, and transparent polymer film with increased mechanical strength.

the particle interstices. Additional work is needed to fully understand the dynamic drying process in film-forming latex suspensions upon evaporation.

In this work we study the dynamic drying process in latex suspension droplets using optical imaging and profilometry. We systematically study the effect of latex concentration on drying dynamics in film-forming suspensions with dispersant concentrations ranging from ultradilute to the concentrated regime (volume fraction $\phi = 1.25 \times 10^{-5}$ to $\phi = 0.40$). In particular, we focus on lateral drying heterogeneities, emergent deformation kinetics, and material properties in film-forming latex droplets. The drying process is studied by continuously monitoring dynamics at the drop edge (initial stages) and the evolution of deposition topology (final state). For these experiments, we directly observe the contact angle θ (Fig. 1) at the drop edge during the drying process, together with independent optical and surface profilometry measurements that provide complementary information on drying dynamics. Interestingly, our results show a nonmonotonic contact-angle decay during the drying process for concentrated latex suspensions and we develop a physical model to explain this unexpected phenomenon. Our results also show that concentrated latex suspensions dry with a pinned particulate contact line together with a receding fluidic contact line. Finally, experimental data are interpreted using analytical models that consider Marangoni flow, contact-line friction, and capillary pressure.

II. MATERIALS AND METHODS

A. Film-forming latex suspensions

We studied the film-formation dynamics of an aqueous suspension of latex particles consisting of a random acrylate copolymer. A custom-made aqueous suspension of latex particles was prepared by The Dow Chemical Company for these studies. The polymer was prepared by emulsion polymerization and consists of a random copolymer of methyl methacrylate (49 wt. %), butyl methacrylate (50 wt. %), and methacrylic acid (1 wt. %), stabilized by 1 wt. % (based on solids) sodium lauryl sulfate (SLS). Potassium persulfate was used as the radical initiator. The final particle size was 85 nm and the system was supplied at 36.67% w/w solids. The glass transition temperature T_g of the latex is approximately 5 °C. The minimum film formation temperature (MFFT) for this material is well below room temperature such that these latex particles readily deform and coalesce when packed in close proximity under ambient conditions [1]. The latex particles are negatively charge stabilized in solution due to terminal sulfate groups on the polymer. The stock formulation at latex volume fraction $\phi = 0.40$ was serially diluted with distilled or deionized water to produce samples spanning four and a half orders in magnitude in concentration to $\phi = 1.25 \times 10^{-5}$. The zero-shear viscosity of the stock latex formulation ($\phi = 0.40$) was measured using a shear rheometer with a concentric cylinder geometry (ARES-G2, TA Instruments) and is 9 cP at 20 °C.

B. Optical imaging and profilometry measurements

Contact angles at drop edges were measured continuously during the drying process using a goniometer (Rame-Hart, resolution $\pm 0.01^\circ$). Dry film heights were measured using a surface profilometer (Dektak 3030). Optical measurements of water evaporation were performed *in situ* using an inverted Zeiss microscope with long working distance objective (Zeiss 5×, numerical aperture 0.16) in bright-field mode. Goniometer measurements and microscopy experiments were performed using a dispersed yellow lamp illumination source such that heating effects were found to be negligible. Drying experiments were performed in ambient conditions in a regulated, environmentally controlled setting. Temperatures and relative humidities were monitored throughout the day to be 19 °C ± 1.5 °C and 18 ± 1%, respectively. To account for any putative variability during drying conditions, at least three independent drying events were measured in a 24-h cycle. The equilibrium surface tension at each concentration was measured using the pendant drop method (Rame-Hart) and reduced in characteristic fashion as a function of surfactant concentration [20], with values ranging from 73 ± 1 mN/m at $\phi = 1.25 \times 10^{-5}$ to 52 ± 0.8 mN/m at $\phi = 0.4$.

III. RESULTS

We began by studying the dynamic contact angle during drying by depositing a small aliquot (5 μL) of a latex suspension on an untreated microscope glass slide (see Fig. 2 and Fig. S1 in [21]). Contact-angle measurements from individual experiments are plotted by first subtracting the long-time plateau angle (at final drying time τ_F), followed by normalizing by the initial (maximum) contact angle (Fig. S1 in [21], inset). For relatively concentrated latex suspensions ($\phi \geqslant 0.025$), we found that individual contact-angle decay curves show two distinct peaks ($P1$ and $P2$) occurring at times τ_{P1} and τ_{P2}, as discussed below. Interestingly, individual contact-angle decay curves (at constant ϕ) were found to collapse onto a master curve when plotting normalized contact angle as a function of dimensionless time $\tilde{t} = t/\tau_{P1}$, where τ_{P1} is the first peak time from an individual contact-angle experiment (Fig. S1 in [21]). Each experimental condition was repeated several times such that results plotted in Fig. 2 are averages over at least three independent drying events. Differences between contact angles on the left and right sides of drying droplets were consistently found to occur within less than 1°, which ensures that samples were not prestressed during fluid ejection and sample preparation. Drops showed only a small variation in average initial contact angle as a function of latex volume fraction (Fig. S2 in [21]) such that the average initial contact angle across all samples is 51° with decreasing variability as latex concentration increased.

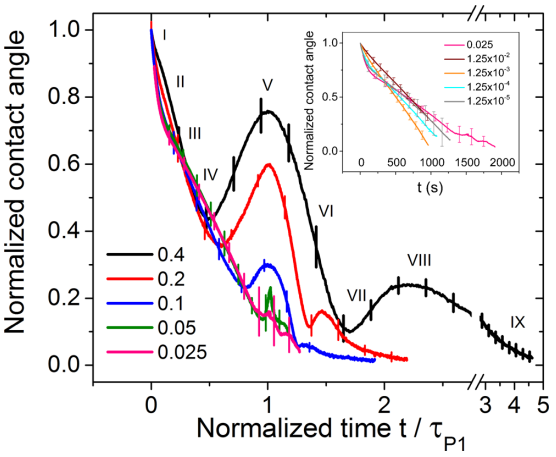

FIG. 2. Nondimensional dynamic contact angle at the drop edge for a drying latex suspension as a function of dispersion volume fraction. Contact-angle data are shown for latex suspensions that exhibit two distinct peaks in contact angles ($\phi \geqslant 0.025$). The graph is nondimensionalized for ease of visualization only and does not affect data analysis. The inset shows contact-angle data for dilute latex suspensions [$\phi = (1.25 \times 10^{-5})$–$(1.25 \times 10^{-2})$] exhibiting only a simple decay in contact angle as a function of time, with the case of $\phi = 0.025$ from the main plot repeated here for reference. This gives a common framework to understand the transition from monotonic to nonmonotonic contact-angle decays as concentration is increased. For all samples, error bars are reported as the standard deviation from at least three independent experiments. Labels I–IX denote the nonmonotonic features in contact-angle decay (shown here for the $\phi = 0.4$ case) and correspond to stages in deposit peak formation, as explained in Fig. 3.

Average normalized contact angles during drying are plotted for a wide range of dispersion volume fractions in Fig. 2. Here we observe two classes of qualitatively different drying dynamics at different latex concentrations as shown in the inset and main plots of Fig. 2. For dilute latex concentrations ($\phi \leqslant 0.025$; Fig. 2 inset), monotonically decreasing contact-angle curves are observed. For the low concentration samples, we observed that the suspensions dry via a pinned fluid line, shown schematically in Fig. 1. For higher latex concentrations ($\phi \geqslant 0.025$; Fig. 2), a strikingly nonmonotonic contact-angle decay response is observed to occur with two distinct peaks. Here the nonmonotonic contact-line decay is accompanied by a *receding fluid line* while packed particles remain pinned at the drop edge at the initial contact line. Error bars in Fig. 2 are calculated as the standard deviation of contact angle from independent measurements. For high latex concentrations ($\phi > 0.025$), all error bars are smaller in magnitude than the primary peak in contact angle.

Before proceeding, we note that our results are based on continuous observation of the contact angle at the pinned drop edge, even for suspensions with high latex concentrations in which the fluid contact line recedes. During the drying process, high-concentration latex dispersions deposit a thick film of latex particles at the dry region of the drop edge, which upon loss of the saturated fluid is often assumed to be completely dry and elastic. However, our results show that the contact angle at the edge responds to the evaporative processes occurring inside the droplet in a noninstantaneous fashion. These results suggest that an elastomechanical coupling occurs within the film-forming material during the drying process (Fig. 1, bottom) and the contact angle at the initial contact-line region is indicative of a transiently drying viscoelastic material. In addition, we observe no discontinuities in the interfacial profile of the drying droplet and no evidence of buckling in the packing front under these conditions [14,19].

Contact-angle decay experiments reveal several intriguing features regarding the film-formation process. First, we find that contact-angle decay curves generally exhibit a similar response at early times. In particular, contact-angle decay curves for dilute latex suspensions ($\phi \leqslant 0.025$)

appear to have similar slopes at the onset of evaporation, indicating negligible effects of dilute latex content on early drying dynamics. This observation holds true even prior to normalizing contact-angle data (Fig. 2, inset) and is expected as all dilute samples generally exhibit similar initial contact angles (Fig. S2 in [21]) and similar final drying times τ_F [Fig. 4(a)]. For concentrated latex suspensions, contact-angle decay curves appear to show common features when plotted as a function of dimensionless time (Fig. 2, main plot), which suggests that these suspensions exhibit some degree of scale-independent evaporative dynamics. In addition, the transition between the two different modes of drying at low versus high latex concentration appears to be smooth, at least as reflected in the transient contact-angle response; in particular, the onset of the nonmonotonic contact-angle decay occurs around $\phi = 0.025$, where the two peaks are comparable in magnitude to the statistical variation between samples. Moreover, upon increasing the latex concentration, the primary and secondary peaks in the transient contact-angle curves appear to be larger in amplitude and occur further apart in dimensionless time during the drying process. Finally, for samples with the highest latex concentrations, the primary and secondary peaks occur earlier in the drying process compared to more dilute suspensions, where peaks occur closer to the terminal decay [see Fig. 4(a), Fig. S7 in [21], and Table S1 in [21]]. These features provide a common framework to analyze drying dynamics, including fluid-line pinning and recession from the contact edge. As denoted in Fig. 2, contact-angle decay curves are labeled with numerals I–IX in order to highlight the origins of these features using optical imaging, as described below.

To understand the origin of the nonmonotonic behavior in contact-angle decay, we performed a series of optical imaging experiments to measure *in situ* deposition patterns, initial contact-line position, and fluid-line position from a top-down viewing perspective. As shown in Fig. 1, when latex particles are suspended in water, light scattering causes the region to appear turbid. As particles begin to pack together but still have a significant amount of water in their interstices ($\phi_{\text{water}} = 0.36$ for random close packed), the mismatch in refractive index adds contrast to the image. Upon continued evaporation, particle voids disappear and particle deformation occurs in the film at temperatures above the MFFT. At this point, the refractive index becomes homogeneous in the sample, leading to a transparent particle layer. This onset of transparency is often used to identify film formation [2].

Figure S3 in [21] shows the optical intensity measured along the radial direction for a latex sample with $\phi = 0.4$ (deposition volume 3 μL). Figure S3A in [21] shows a mostly turbid droplet with a bright edge and the fluid line is identified as a peak in intensity due to changes in refractive index. In this way, the fluid line is observed to move radially inward with increasing time (Figs. S3A–S3C in [21]). The receding fluid line leaves behind a random close-packed bed of particles with water in their interstices (Figs. S3B and S3C in [21]), which upon evaporation gains optical transparency (Fig. S3D in [21]). The film becomes clear when interparticle voids become smaller than the wavelength of light, which occurs in the absence of water in the interstices via a dry-moist sintering mechanism. We note that this is amounts to an inhomogeneous drying regime of a receding water front, which is discussed for the case of latex films in prior work [2]. Here particles are significantly deformed by capillary deformation below the laterally traveling meniscus, while final film formation only occurs by dry-moist sintering on the other side of the traveling meniscus. We further confirmed the motion of fluid line away from the film-forming interface using multicomponent, three-dimensional fluorescence confocal microscopy as shown in Fig. S4 in [21]. In these experiments, Alexa 408 dye (blue color) was suspended in water while latex particles were labeled Nile red dye (red color). During drop drying, latex particles accumulate at the drop edge, with the Nile red fluorescence intensity increasing in the increasingly apolar environment devoid of water, whereas the water front moves radially inward towards the end of drop drying. Overall, this experiment provides direct evidence for fluid-line recession in concentrated latex suspensions that remains common due to the close packing of latex spheres at drop edge in both systems.

Importantly, our results show that contact-angle nonmonotonicity is only observed in latex suspensions that exhibit lateral heterogeneity in drying, that is, suspensions in which the fluid line recedes and the drop edge dries before the drop center. Moreover, we find that the bulk of the dry region at the droplet edge left behind by a receding fluid line responds as a viscoelastic solid, in

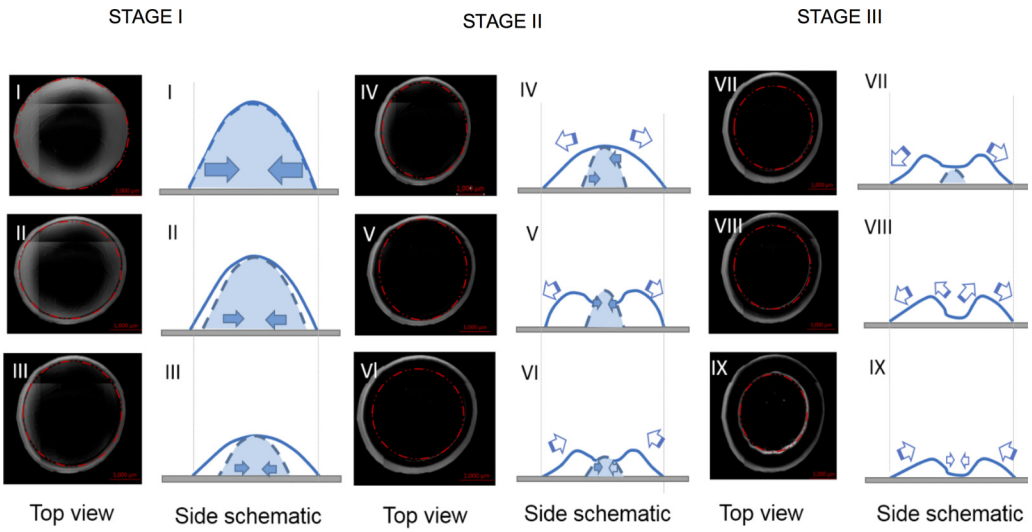

FIG. 3. Schematic of three distinct stages during drying for dispersions with high latex concentration. In stage 1, the fluid line recedes and the contact angle monotonically decays. In stage 2, formation of the dry outer edge leads to expansion and contraction of the *outer* interface, causing a peak in contact angle at time τ_{P1}. In stage 3, the inner crater of a volcanolike topology forms and depletion of water here expands and contracts the inner interface, subsequently resulting in a secondary peak in contact angle at time τ_{P2}. In optical micrographs, the dashed red line indicates the fluid-line position. In schematic images, the solid blue line represents the responsive particle-rich interface (open arrows) that introduces contact angle-peaks and the dashed blue line represents the fluid interface shown to constantly recede (filled arrows). Roman numerals I–IX correspond to stages in two-peaked contact-angle decay curves common to all high concentrations, shown in Fig. 2 for the case of $\phi = 0.4$.

the sense that this behavior suggests a noninstantaneous response to drying stresses, as explained in Sec. IV A and supported by prior work [2,22].

The drying process for a high-concentration latex suspension is shown schematically in Fig. 3, along with corresponding optical micrographs of deposition patterns. Based on these results, we identify three stages of drying. Stage 1 corresponds to the initial contact-angle decay at early times, wherein the fluid line recedes from the drop edge. Here the solution continues to deposit latex particles at the edge, resulting in the rapid deposition and buildup of an inclined material interface, which ultimately forms a particle-rich region near the periphery with a smooth slope. During this stage of evaporation, the liquid drop height continuously reduces, causing a rapid decay in initial contact angle that is similar to dilute dispersion drying, as shown in Fig. 1 for the pinned contact-line case. In stage 2, a dry region begins to form at the drop edge where packed particle beds are nearly devoid of water, which is shown schematically in Fig. 1, bottom. During this stage, the contact angle is observed to increase, followed by a subsequent decrease, resulting in a primary peak $P1$ at time τ_{P1} (Fig. 2 and Fig. S1 in [21]). This nonmonotonic behavior is attributed to a dilational stress buildup and stress relaxation, as explained in Sec. IV A. Finally, stage 3 begins with the formation of the inner crater of a volcanolike surface topology, wherein the droplet center is nearly devoid of water due to evaporation. Here the emergent inner interface again responds to depletion of water, thereby resulting in the secondary peak $P2$ in contact angle at time τ_{P2}. However, given the increased rigidity of nearly dry film at this stage of the drying process, the second breathing mode generates less strain and the magnitude of the second peak is less than the primary peak.

The volume fraction dependence of the average values of the final drying time τ_F, the first peak time τ_{P1}, and relative second peak time τ_{P2}/τ_{P1} is shown in Fig. 4(a). We further plot final drying times per unit volume of water $\tau_F' = \tau_F / V_w$, where V_w is the water volume, in order to account for

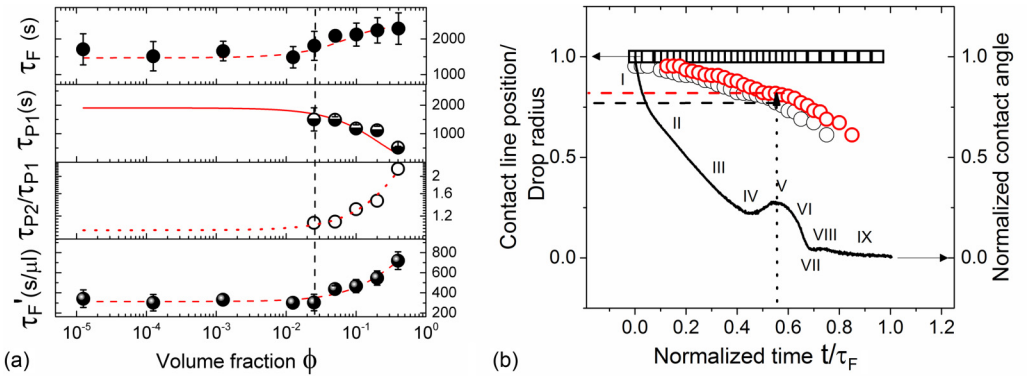

FIG. 4. Quantitative analysis of absolute time scales and receding fluid-line position during latex droplet drying. (a) Average time scales associated with contact angle are plotted as a function of dispersion volume fraction ϕ, including final drying time τ_F, primary peak time τ_{P1}, relative secondary peak time τ_{P2}/τ_{P1}, and final drying time relative to water volume in the droplet $\tau_F' = \tau_F/V_w$. The dashed vertical line shows the transition from the dilute regime to the concentrated regime. (b) Quantitative analysis of receding fluid-line position during droplet drying. Initial contact-line position (black squares) and receding fluid-line position (black circles) are plotted normalized to the drop radius (1.51 mm) for a $\phi = 0.1$ latex dispersion. Here the time axis is normalized to the final drying time τ_F because peak formation time is not evident from (purely) optical imaging experiments. The position of the receding fluid line is further plotted with a time delay of 10% of the total drying time (red circles), which leads to good correspondence with the different stages in contact-angle decay (black line), as described in the text. Time points shown with roman numerals correspond to stages of deposit evolution shown in Fig. 3.

differences across sample concentrations. The vertical dashed line in Fig. 4(a) marks the transition from the dilute to nondilute latex concentration regime at $\phi = 0.025$. For dilute suspensions, all time scales are relatively constant as a function of latex volume fraction. At higher concentrations, the final drying time τ_F generally shows a moderate increase with an approximately exponential response and the first peak time τ_{P1} decays exponentially. Interestingly, the absolute second peak times τ_{P2} vary only slightly (not shown), but the relative delay between peaks $P2$ and $P1$, represented by τ_{P2}/τ_{P1}, increases linearly upon increasing latex concentration. The volume fraction dependence of peak amplitudes for $P1$ and $P2$ shows that the magnitudes of contact-angle peaks at $P1$ and $P2$ increase at higher concentrations (Fig. S5 in [21]), which we show to be due to the increased ratio of local viscosity to elasticity in Sec. IV A. Finally, the data in Fig. 4(a) show that the ratio of the first peak time τ_{P1} to the final drying time τ_F rapidly decreases upon increasing latex volume fraction. As the fluid line recedes faster for high-concentration suspensions, $P1$ occurs relatively faster (Fig. S7 and Table S1 in [21]) in the drying process, which makes the first peak time τ_{P1} a convenient parameter to characterize the degree of drying heterogeneity. On the one hand, an increase in the drying time τ_F is a generally desirable feature for a latex suspension (potentially resulting in longer open times), however, our experiments show this is accompanied by an undesirable increase in heterogeneity, as discussed below.

Primary and secondary peaks in contact angle occur as an emergent response to fluid-line recession, which creates outer and inner particle-rich interfaces. Interestingly, we find that the contact-angle response (labeled with numerals I–IX in Fig. 2) occurs after a short-time delay compared to fluid-line recession (labeled with numerals I–IX in Fig. 3). In particular, we tracked the position of the receding fluid line (dotted red line in Fig. 3), which provides the location of the inner edge of the particle-rich dry region. In order to make a quantitative comparison, we analyze the travel time of the fluid line past the primary peak in the deposition pattern (optical micrograph, panel V, Fig. 3) in comparison to the primary peak formation time in contact-angle decay (corresponding to time point V in Fig. 2).

In Fig. 4(b) the dynamic fluid-line position (black circles) is plotted together with the pinned particulate contact line (black squares), which is characteristic of the simultaneous pinning and receding phenomena observed in this study for all concentrated suspensions drying with lateral heterogeneity. It is noteworthy that the dry region at the drop edge continuously responds to contact-angle decay, but the contact line refrains from receding and remains pinned throughout drying. Also plotted in Fig. 4(b) is the contact-angle decay (black line) for the $\phi = 0.1$ suspension for the same relative drying time. These results show that when the drop edge exhibits a peak (at point V), the fluid line has traveled approximately 75% of the drop radius. However, the position of the peak in the dry deposition is at approximately 83% of the drop radius, as determined by profilometry measurements. These results suggest that the particle-rich interface responds to fluid-line recession with a delayed contact-angle response. In other words, by the time the contact angle reaches its peak, the fluid line has already receded beyond the film deposition peak. The receding fluid line can be considered as the stimulus driving the contact-angle response because the recession creates a heterogeneous dry region with new material properties. This is also supported by the fact that the inner rim of the deposition pattern appears in optical micrographs at the end of stage 2, whereas the contact-angle response for the secondary peak only appears in stage 3. We hypothesize that the time delay arises due to the viscoelastic nature of the colloidal suspension undergoing drying. To probe this further, we plotted the fluid-line recession data with a 10% relative time delay [Fig. 4(b), red circles], which results in a match between the contact-angle peak response and fluid-line position above the physical film peak. In this way, we roughly estimate that the response time of the dry region material should be around 10% of the total drying time ($\tau_{\text{delay}} \approx 216$ s) for this sample under these drying conditions.

A delay between a physical stimulus and response is a signature of the viscoelastic nature of some complex fluids [22,23] and gains significance here as the dry region at drop edge has the highest latex concentration within the droplet. Given the dynamic nature of evaporation from a suspension, experimental measures of transient rheological properties remain difficult to obtain for these materials [22]. Here we interpret the time delay as an average transient relaxation time of the viscoelastic dry front during peak formation. It would be interesting to study the dependence of the time delay for higher-latex-concentration suspensions using this kinetic method, but tracking the fluid line through opaque deposit peaks at higher latex concentrations is challenging. Nevertheless, the fluid-line recession dynamics serves to delineate the nature of the unique nonmonotonic contact-angle decay observed in our experiments. Moreover, evidence of a response delay also further establishes polymer deposit peak formation as the consequence of stimulus of receding fluid-line dynamics. This knowledge paves the way forward to determine average contact-line recession velocities for all samples studied here as described in the following section.

We further sought to investigate the relationship between lateral drying heterogeneity and surface deposition topology (Fig. 5). It is known that the interplay between fluid contact-line recession and material deposition onto a substrate results in either a volcanolike topology [7] or a mountainlike topology [24]. According to pioneering work on coffee-ring effects [15] and more recent work [4], a pinned fluid line is required to produce a coffee-ring deposition pattern. When the fluid line remains pinned at the drop edge, material is continuously deposited at the particle front, thereby yielding a coffee-ring deposition pattern. On the other hand, for receding fluid lines, the interplay between the rate of fluid-line recession and the rate of material deposition determines the shape of the deposition topology and the location of any putative deposition peak(s). Qualitatively, if the fluid line rapidly recedes, then particle deposition is observed to occur at the center, thereby resulting in a mountainlike deposit. However, if the fluid line recedes slowly, then a deposition peak will appear between the edge and the center, thereby yielding a volcanolike deposition pattern [10].

Based on this reasoning, we hypothesized that a smooth transition between coffee-ring deposits to volcanolike or mountainlike deposits would occur in these film-forming systems. Indeed, optical micrographs show a coffee-ring pattern [Fig. 5(a)] for the ultradilute concentration regime and a volcanolike topology for higher latex concentrations. The profile of the deposited film was measured using surface profilometry and is plotted for both low- and high-latex-concentration regimes in

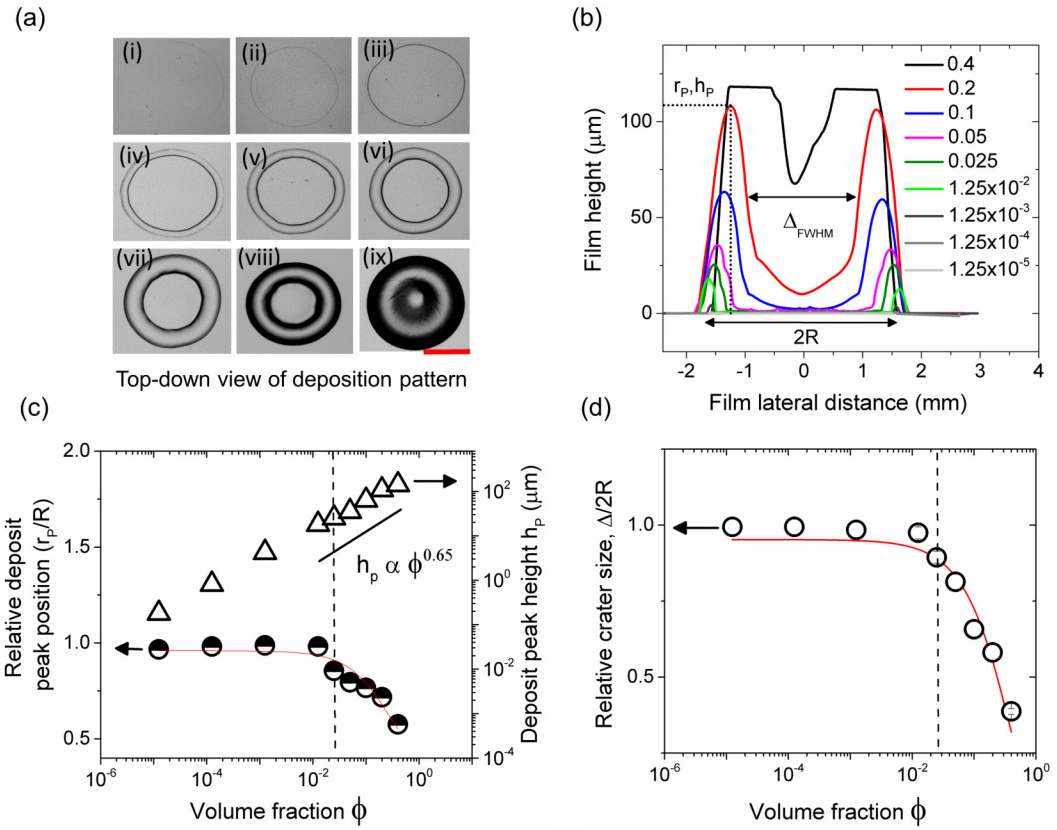

FIG. 5. Dependence of latex concentration on deposition patterns. (a) Optical micrographs (top-down view) of dry-film patterns for latex dispersions with varying ϕ: (i) 1.25×10^{-5}, (ii) 1.25×10^{-4}, (iii) 1.25×10^{-3}, (iv) 1.25×10^{-2}, (v) 0.025, (vi) 0.05, (vii) 0.1, (viii) 0.2, and (ix) 0.4. The scale bar is 1.5 mm. (b) Surface profilometry data showing radial dependence of film height. Truncated peaks for the $\phi = 0.4$ sample arise due to instrument range limitations. (c) Deposit peak position and height as a function of latex volume fraction. The ratio of peak position of deposit maximum r_p relative to drop radius R (half filled circles) shows an exponential decay (red line, exponential fit). Open triangles show peak height of the dry film pattern h_p, which obeys a power-law relationship with volume fraction ϕ such that $h_p \propto \phi^{0.65}$. (d) Relative crater size in volcanolike deposits and receding fluid-line velocity as a function of ϕ. The ratio of crater size to deposit diameter $\Delta_{\mathrm{FWHM}}/2R$ (open circles) shows single-exponential decay (red line, exponential fit). Vertical dashed lines in (c) and (d) demarcate the dilute and concentrated regimes.

Fig. 5(b). In the limit of high latex concentration, the deposition topology shows a peak away from the drop edge and a depressed crater in the center, indicative of a volcanolike topology. The lower concentration regime samples are confirmed to give a coffee-ring-like profile (Fig. S6 in [21]), where the deposition peak is located closer to the drop edge.

Returning to the profilometry data in Fig. 5(b), we identify three parameters of interest: film height at the deposition peak h_p, the distance between the peak and the drop center r_p, and crater size Δ_{FWHM}, defined as the full width at half maximum between the peaks of the volcano. Peak height h_p and peak position r_p are plotted in Fig. 5(c) for all samples. Our results show that in the high-concentration regime, peak position r_p decays exponentially, whereas peak height h_p follows a power-law response with latex volume fraction ϕ according to $h_p \propto \phi^{0.65}$. Interestingly, peak height appears to have a continuous functional dependence on latex volume fraction, with a smooth transition between the coffee-ring and volcanolike surface deposition regimes. Finally, the

deposit profile is important for several lithographic applications [7] and thus the ratio of the crater size Δ_{FWHM} to drop diameter $2R$ is further plotted in Fig. 5(d). Here we find that the quantity $\Delta_{\mathrm{FWHM}}/2R$ is unity for a coffee-ring deposit, which transitions to a simple exponential relationship with ϕ for higher latex concentrations.

IV. ANALYSIS AND DISCUSSION

A. Analytical model for contact-angle nonmonotonicity

In this section we develop an analytical model to explain the nonmonotonic contact-angle decay for drying drops of concentrated latex suspensions. This model is based on the development of a dilational stress in the early stages a drying droplet of latex particles [22]. During stage I of drying (Fig. 3), latex particles are convected toward the droplet edge and a packing front of particles begins to form. In this stage of drying, the fluid exerts a viscous drag onto the particle network, which induces an internal elastic stress in the particles. Realistically, the stress is likely manifested by only minor strains due to particle compression in the interstices near the particle-particle contact points. When the fluid line begins to recede, the dilational stress is released, thereby resulting in a lateral expansion of the preformed particle network and a concomitant increase in the contact angle (stage II, Fig. 3). However, the release of stress is a transient process and the contact angle continues to decay as the drop continues to dry. Together, this process results in a nonmonotonic contact angle and a peak in the transient contact angle during drying. In this section we analytically model this process by first performing a mass balance to estimate the magnitude of the dilational stress, followed by modeling the stress relaxation using a viscoelastic solid (Voigt element).

1. Pressure and dilational stress in a drying droplet

We begin by performing a mass balance of solvent flowing through the compacted region. For our experiments, the outer drop edge is constant at R_0, $H(t)$ is the drop height at the radial center of the drop, and s is the arc length along the air-liquid interface from r_f to R_0. The drop is assumed to dry at a continuous but constant rate $\dot{E}$ as shown in Fig. 6(a). The droplet height profile is assumed to be parabolic:

$$h(r,t) = H(t)\left(1 - \frac{r^2}{R_0^2}\right). \tag{1}$$

From an arbitrary position r to R_0, the arc length s is given by

$$s(r) = \int_r^{R_0} \sqrt{1 + \left(\frac{dh}{dr'}\right)^2}\, dr'. \tag{2}$$

The arc length can be computed numerically by substituting dh/dr from Eq. (1),

$$s(r) = \int_r^{R_0} \sqrt{1 + \left(\frac{4H^2(t)r'^2}{R_0^4}\right)^2}\, dr'. \tag{3}$$

The fluid velocity in the radial direction due to evaporation is u_r such that $u_r > 0$ for $r > 0$. By Darcy's law, fluid velocity is related to pressure within the region $p(r)$,

$$u_r(r) = \frac{-k_p}{\mu}\frac{dp}{dr}, \tag{4}$$

where μ is the fluid viscosity and k_p is the permeability of the particle bed. This relation implies that the pressure decreases as the radial distance increases from the drop center such that $dp/dr < 0$ for $r > 0$.

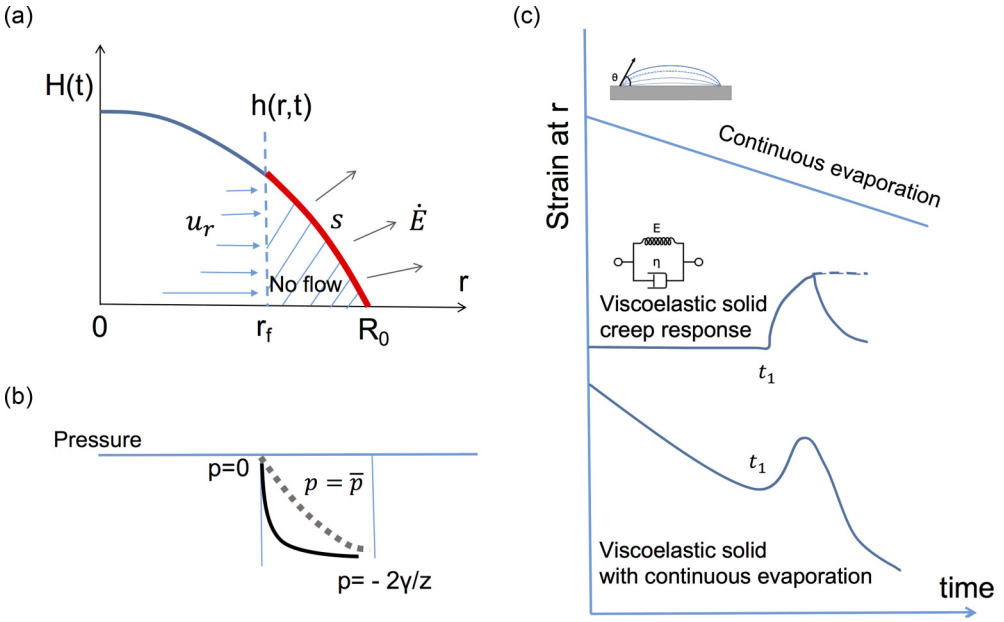

FIG. 6. Analytical model for nonmonotonic contact-angle decay. (a) Geometry and height profile of a drying droplet with packing front located at r_f, with a fluidic region to the left and a compacted region to the right. (b) Pressure in the compacted region at the instant the fluid line begins to recede. The dotted line shows a qualitative sketch of the pressure distribution from Eq. (6) and $\bar{p}$ is the average pressure. The solid line shows the approximation of capillary pressure sustained by the particle network. (c) Strain response plotted for three cases of continued evaporation of the dilute limit (top panel), viscoelastic solid creep-recovery response upon application of a transient step stress from t_1 to $t_{\max}$ (middle panel), and a linear superposition of the continued evaporation and creep response (bottom panel).

Fluid moving across a vertical plane at an arbitrary position r must evaporate across the air-liquid interface of length s. Performing a mass balance gives

$$u_r(r)h(r) = \frac{k_p}{\mu}\frac{dp}{dr}h(r) = s(r)\dot{E}, \tag{5}$$

where $h(r)$ is given by Eq. (1), $s(r)$ is given by Eq. (3), and $\dot{E}$ has units of volumetric flow rate (per unit length and drop height). In this way, pressure $p(r)$ can be calculated as

$$p(r) = \int \frac{\mu \dot{E}}{k_p}\frac{s(r)}{h(r)}dr + C, \tag{6}$$

where C is a constant of integration with the boundary condition defined as $p = 0$ at $r = r_f$. This expression is qualitatively sketched in Fig. 6(b) as the dotted line. The average pressure due to fluid flow from $r_f \leqslant r \leqslant R_0$ is

$$\bar{p} = \frac{1}{R_0 - r_f}\int_{r_f}^{R_0} p(r)dr. \tag{7}$$

The dilational stress is approximately given by $\sigma_s = \bar{p}h(r_f,t)$, which assumes that the stress is a surface stress (units of force per length). An alternative (and simpler) method for estimating the dilational stress is to assume that the average pressure should be of the same order of magnitude as the capillary pressure [22]. In other words, the maximum pressure that the particle bed can support

is equivalent to the capillary pressure

$$\bar{p} = p_{\text{cap}} = \frac{2\gamma}{z}, \tag{8}$$

where γ is the water-air surface tension and z is the radius of curvature of the menisci in the particle interstices. The curvature z is usually taken to be $0.1d$, where d is the particle diameter [22]. In this case, it is assumed that the capillary pressure dominates as the average pressure over the region of interest [22] and the response for this case is qualitatively sketched as a solid line in Fig. 6(b). The negative pressure at the drop edge compared to the zero pressure at the center leads to a dilational stress σ_s experienced by the compacted region of latex particles. In either case, calculating the pressure using Eq. (6) or the capillary pressure approximation, the general form of the average pressure is monotonically decreasing with the largest (negative) magnitude at the edge. Finally, we can approximately estimate the bulk stress σ_0 using the capillary pressure expression in Eq. (8) as $\sigma_0 = 17.5$ MPa, which agrees with previous estimates [22]. A surface tension of 35 mN/m for water saturated with surfactants near the compaction point is consistent with prior work [22] and with our surface-tension experiments.

2. *Droplet strain and contact angle in the early-time limit*

In the early stages of drying, the contact angle decreases monotonically due to evaporation. We begin by considering the simple case of early-time evaporation and simple contact-angle monotonic decay. As shown in Fig. 6(a), the drop is assumed to have a parabolic geometry given by Eq. (1). The rate of change of drop height $H(t)$ at the center of drop is

$$h(0,t) = H_0 - \dot{E}t, \tag{9}$$

where $H_0 = h(0,0)$. The contact angle is given by

$$\theta(t) = \frac{2h(0,t)}{R_0} = \frac{2}{R_0}(H_0 - \dot{E}t). \tag{10}$$

A characteristic time scale for evaporation time can be written as

$$\tau_{\text{ev}} = \frac{V_0}{|\dot{V}_0|} = \frac{(\pi/2)H_0R_0^2}{(\pi/2)\dot{H}_0R_0^2} = \frac{H_0}{\dot{E}}, \tag{11}$$

where V_0 is the initial drop volume. Using this approach, we can define drop strain during continued evaporation as

$$\gamma(t) = \frac{h(0,t)}{H_0} = \frac{\theta(t)}{\theta_0} = 1 - \frac{t}{\tau_{\text{ev}}}. \tag{12}$$

In the limit of pinned contact line (constant drop radius R_0) and continued evaporation strain can expressed as

$$\gamma(t) = \frac{\theta(t) - \theta_f}{\theta_0 - \theta_f} = 1 - \frac{t}{\tau_{\text{ev}}}, \tag{13}$$

where the final angle is θ_f. It follows that at early times, drop evaporation proceeds by a simple strain response with a monotonic decrease in contact angle with a characteristic rate of $1/\tau_{\text{ev}}$. We refer to this stage as the continuous evaporation limit, and this is shown schematically in Fig. 6(c) (top panel). This linear decay is observed in dilute concentration latex suspensions as shown in Fig. 2 inset. This implies that in the dilute limit and during early stages of evaporation for high-concentration latex suspensions, initial evaporation rates are similar, which explains our observation of similar initial slopes shown in Fig. 2 (inset).

3. Nonmonotonic strain response

Based on the contact-angle decay for the high-concentration latex suspensions (Fig. 2), we viewed this process as a transient creep and inelastic recovery experiment, which is consistent with the application of a transient constant stress. This type of strain response is often modeled using a viscoelastic solid or Voigt model [23], which forms the basis of the analytical model in this section. The choice of modeling the compacted region as a viscoelastic solid distinguishes this work from the prior work [22] where the compacted particles were assumed to be purely elastic. The viscoelastic nature of the compacted region behavior is consistent with our optical imaging experiments (Fig. S4 in [21]), which show that a purely dry film is not observed until the final drying time. Thus water is retained in the interstices of the compacted region in stages I and II of the drying process.

The standard viscoelastic solid element to model the accumulated strain and retarded recovery is the Kelvin-Voigt element, shown schematically in Fig. 6(c) (middle panel). The Voigt model consists of a spring with a modulus E in parallel connection to a dashpot representing a viscous element with viscosity η. An applied stress is distributed between these elements at time $t = t_1$ such that

$$\sigma_{\text{total}} = \sigma_0 = E\gamma + \eta\dot{\gamma}, \tag{14}$$

where γ is the strain. This linear, nonhomogeneous differential equation can be solved to give the strain response of a viscoelastic solid

$$\gamma(t) = \frac{\sigma_0}{E}\left[1 - \exp\left(\frac{-(t - t_1)}{\tau_r}\right)\right] \quad \text{for } t_1 < t < t_{\max}, \tag{15}$$

where $\tau_r = \eta/E$ is the relaxation time (or retardation time) of the viscoelastic solid and t_1 is the time at which the dilational stress σ_0 is applied. When the applied stress is removed at $t = t_{\max}$, the strain recovers as

$$\gamma(t) = \frac{\sigma_0}{E}\exp\left(\frac{-t}{\tau}\right)\left[\exp\left(\frac{t_{\max}}{\tau}\right) - \exp\left(\frac{t_1}{\tau}\right)\right] \quad \text{for } t > t_{\max}. \tag{16}$$

Equations (15) and (16) give a characteristic delayed strain accumulation response as shown in Fig. 6(c) (middle panel). It is evident that the continuous evaporation effect from Eq. (12) together with the creep recovery strain in Eq. (15) for the compacted region qualitatively captures the nonmonotonic contact-angle strain observed in our experiments. In Fig. 6(c) (bottom panel), the sum of these effects is qualitatively sketched. We now proceed to a more quantitative model for these phenomena.

Combining Eqs. (12) and (15) yields the total strain in a drying drop of film-forming latexes with constant stress σ_0 applied from t_1 to $t_{\max}$:

$$\gamma(t) = \begin{cases} 1 - \frac{t}{\tau_{\text{ev}}}, & t \in (0, t_1) \\ 1 - \frac{t}{\tau_{\text{ev}}} + \frac{\sigma_0}{E}\left[1 - \exp\left(\frac{-(t-t_1)}{\tau}\right)\right], & t \in (t_1, t_{\max}). \end{cases} \tag{17}$$

The strain rate is given by

$$\frac{d\gamma(t)}{dt} = \begin{cases} -\frac{1}{\tau_{\text{ev}}}, & t \in (0, t_1) \\ -\frac{1}{\tau_{\text{ev}}} + \frac{\sigma_0}{E\tau}\exp\left(\frac{-(t-t_1)}{\tau}\right), & t \in (t_1, t_{\max}). \end{cases} \tag{18}$$

The primary peak time τ_{P1} and peak strain γ_{P1} can be obtained by differentiating Eq. (17) or using the strain rate expression given by Eq. (18):

$$\tau_{P1} = -\tau \ln\left[\frac{\tau E}{\tau_{\rm ev}\sigma_0}\exp\left(\frac{-t_1}{\tau}\right)\right],$$
$$\gamma_{P1} = \left(1-\frac{\tau_{P1}}{\tau_{\rm ev}}\right)+\frac{\sigma_0}{E}\left[1-\exp\left(\frac{-(\tau_{P1}-t_1)}{\tau}\right)\right]. \tag{19}$$

Using this approach, the primary peak time τ_{P1} can be predicted with knowledge of the materials properties.

4. Results from the analytical model and validation

Equations (17) and (18) describe the evolution of the drying drop for early and intermediate times during the evaporation process. These equations successfully capture the early-time contact-angle decay and the intermediate-time nonmonotonic contact-angle response for drying drops of concentrated latex suspensions. With knowledge of the materials properties, Eq. (19) can be used to predict the primary peak time τ_{P1}. In practice, however, it is difficult to accurately determine all of the materials properties (modulus E, rate of evaporation $\dot{E}$, magnitude of dilational stress σ_0, and viscosity η) during the transient drop-drying event for a series of different latex concentration suspensions. As an alternative approach, we use the analytical framework to interpret our experimental data by self-consistently determining a few of these parameters for our system. In this approach, Eq. (18) can be used to determine the unknowns $\tau_{\rm ev}$, τ, and σ_0/E if it is applied to two different time points during the drying process such that material properties are nearly constant. The results can then be used validate this model in a self-consistent way using Eq. (19) by comparison to experimental observations of primary peak strain.

In Figs. 7(a) and 7(b), an average transient strain $\gamma(t) = \theta(t)/\theta_0$ and corresponding strain rate $\frac{d\gamma(t)}{dt}$ are plotted for the $\phi = 0.40$ suspension. Similar strain decays for other latex concentration suspensions are plotted in Fig. S7 in [21]. Applying Eq. (18) to the early-time regime $t \in (0,t_1)$, we estimate $\tau_{\rm ev} = 1500$ s, as shown by the dashed gray line in Fig. 7(a). Similarly, applying Eq. (18) to the intermediate-time region $t \in (t_1,t_{\rm max})$ and solving for two different time points at $t = t_{s1}$ and $t = t_{\rm max}$ yields

$$\tau = \frac{t_{\rm max}-t_{s1}}{\ln(\tau_{\rm ev}\dot{\gamma}_{s1}+1)}, \quad \frac{\sigma_0}{E} = \frac{\tau}{\tau_{\rm ev}}\exp\left(\frac{t_{\rm max}-t_1}{\tau}\right), \tag{20}$$

where $\dot{\gamma}_{s1} = d\gamma/dt$ at time $t = t_{s1}$, as shown in Fig. 7. Using Eq. (20) for the $\phi = 0.40$ case, we obtain estimates for $\tau = 300$ s and $\sigma_0/E = 0.46$. Using these parameter estimates in Eq. (19) yields an estimate for the peak strain $\gamma_{P1}^{\rm calc} = 0.95$ compared to an experimentally determined value of the peak strain of $\gamma_{P1} = 0.93$, as shown in Fig. 7(a). This suggests that the model is providing reasonable estimates for the experiments.

This process was followed for the high-concentration latex suspensions and the results are tabulated in Table S1 in [21]. Figure 7(d) shows a comparison between γ_{P1} determined from the experiments and the analytical model, generally showing good agreement. In Fig. 7(c), retardation times τ are plotted as a function of latex concentration, showing that around a latex volume fraction of $\phi = 0.025$, the retardation time τ decreases. This observation is consistent with data in Fig. 2, where the peaks in contact angle become uncharacteristically sharp for $\phi > 0.025$. We further note that estimates of the elastic modulus E and viscosity η from the analytical model are in reasonably good agreement with the modulus and zero-shear viscosity estimate for a film of water-based latex particles undergoing drying with the water receding mechanism [2,25,26].

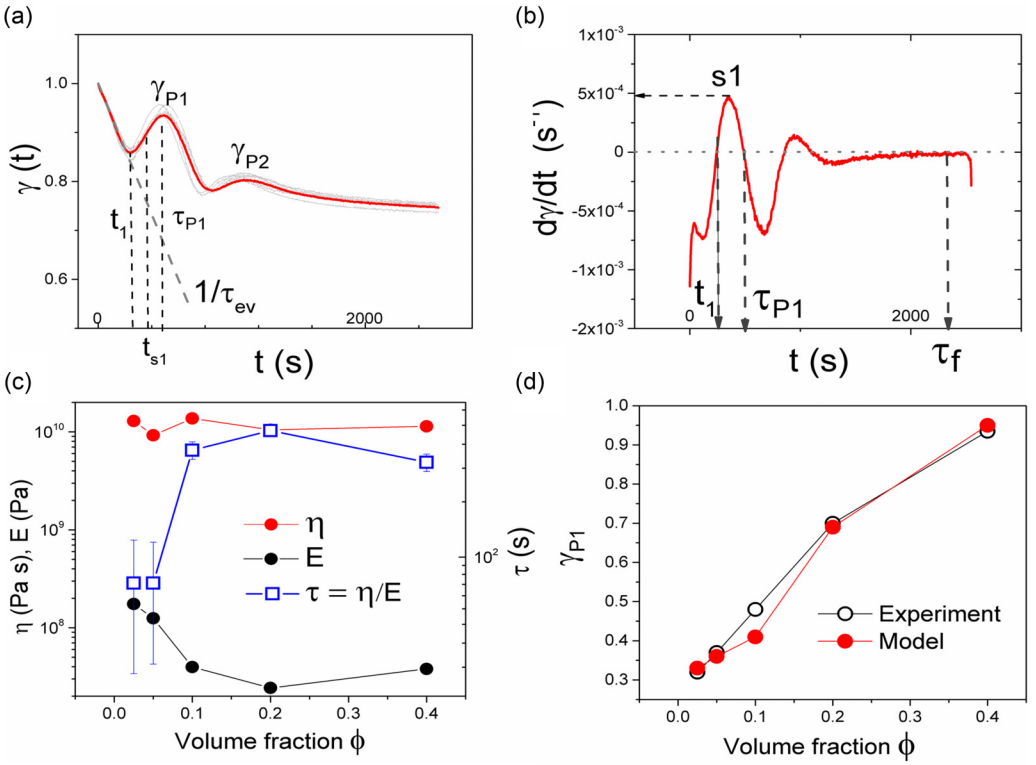

FIG. 7. Results from the analytical model for drying latex suspensions. (a) Strain $\gamma = \theta(t)/\theta_0$ as a function of time for the latex suspension with volume fraction $\phi = 0.40$. The gray dashed line represents the initial rate of evaporation in the continual evaporation (low latex concentration) limit. The experimental strain curve is used to estimate system parameters, as explained in the text. (b) Average strain rate $d\gamma/dt$ for the latex suspension with volume fraction $\phi = 0.40$. (c) System parameters obtained for different latex volume fraction samples, including modulus E, viscosity η, and retardation time τ for the compacted particle region. Error bars arise from statistical differences in averaged strain responses. (d) Peak strain γ_{P1} determined from the analytical model and experiments.

B. Factors affecting drying heterogeneity and their concentration dependence

In the following section, we aim to explore the physical origins of lateral drying heterogeneity. Fluid-line recession is thought to be affected by three factors. (i) The first is Marangoni flow, wherein surface-active species such as surfactants exhibit a concentration gradient at the liquid-air interface due to capillary flow-induced preferential deposition at drop edge. Here the surface gradient in surfactant concentration induces a Marangoni flow towards the droplet center, which aids in fluid-line recession [3,6,27]. (ii) The second is fluid flow through the packed bed of particles, wherein dense particle packing at the droplet edges induces a relatively high resistance to fluid flow, causing a high-pressure drop required to sustain fluid flow towards the drop edges. Here the fluid line recedes when the requisite pressure drop in the packed bed exceeds the opposing capillary pressure holding water in the particle interstices at the drop edge [11,12]. (iii) Third is reduced contact-line friction, which results from a change in surface wetting properties due to film deposition that leads to fluid-line recession [4]. In the following, we investigate the roles of these mechanisms using a comprehensive approach that aims to establish their relative influence on drying heterogeneity in our system. For comparative purposes, the average primary peak formation time τ_{P1} is correlated with key parameters from these distinct mechanisms.

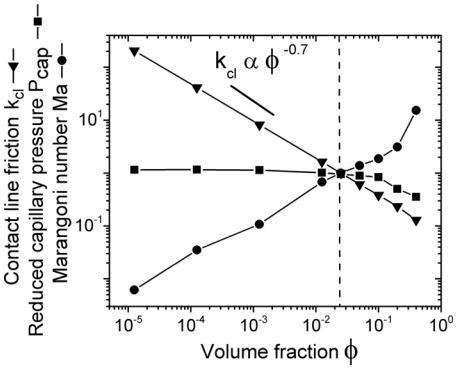

FIG. 8. Factors affecting fluid-line recession and onset of lateral drying heterogeneity, including scaled Marangoni number Ma′ (circles), reduced capillary pressure (squares), and contact-line friction coefficient (triangles) as a function of dispersion volume fraction ϕ. The contact-line friction constant k_{cl} is calculated from Fig. S9 in [21] as a function of ϕ based on the theory described in Ref. [4] and is found to have a simple power-law dependence on latex volume fraction ϕ such that $k_{\mathrm{cl}} \propto \phi^{-0.7}$. The vertical dashed line denotes the transition between the dilute and concentrated regimes.

C. Marangoni flow

For dilute latex suspensions, our results show the emergence of the coffee-ring effect in deposition images [Figs. 5(a) (i)–5(a) (iv)]. Prior work has sought to suppress or entirely avoid the coffee-ring effect by inducing Marangoni flows, which tend to counter deposition at the edges of drops by transporting particles toward the drop center [3,5,15]. It is possible that Marangoni flows could explain the decrease in crater size to drop diameter $\Delta_{\mathrm{FWHM}}/2R$ upon increasing latex volume fraction, as shown in Fig. 5(d). The relative strength of surface-tension forces to viscous forces is given by the dimensionless Marangoni number Ma [3,6],

$$\mathrm{Ma} = \frac{\Delta\gamma L}{\eta D}, \tag{21}$$

where L is the characteristic length scale over which a surface tension gradient $\Delta\gamma$ exists, D is the diffusion constant of the interfacially active species, and η is the solution viscosity. The equilibrium surface tension for the latex suspension in this work ranged from 73 to 48 mN/m for ultradilute ($\phi = 1.25 \times 10^{-5}$) to concentrated latex suspensions ($\phi = 0.4$), respectively. Here we assumed that the center of the droplet has a surface tension corresponding to the ultradilute latex concentration, whereas the droplet edge has a surface tension corresponding to the equilibrium surface tension for the respective latex concentration. This is a common assumption for determining surface-tension gradients [6], as it is generally quite challenging to directly measure *in situ* surface-tension gradients. For comparison purposes, data are analyzed using a rescaled Ma such that the Marangoni number is scaled to the value of $\mathrm{Ma}_{\mathrm{crit}}$ at the dilute to concentrated transition ($\mathrm{Ma}_{\mathrm{crit}} = 3 \times 10^6$ for latex suspension with $\phi = 0.025$, $\Delta\gamma = 13$ mN/m, and $L = 100$ μm). In this way, we consider relative changes in Marangoni number with increasing concentration. In Fig. 8 we plot the rescaled Marangoni number $\mathrm{Ma}' = \mathrm{Ma}/\mathrm{Ma}_{\mathrm{crit}}$ as a function of latex volume fraction, which shows that Ma increases by approximately three orders of magnitude for a corresponding increase of five orders of volume fraction.

We next plot the primary peak time τ_{P1} relative to the final drying time τ_{P1}/τ_F as a function of Ma′ (Fig. 9, top panel). Interestingly, our results show a power-law relationship for the primary peak time τ_{P1} as a function of Ma′ such that $\tau_{P1}/\tau_F \propto \mathrm{Ma}^{-0.5}$. The analysis shows that an increase in interfacial Marangoni flows above the critical value is associated with smaller primary peak times times τ_{P1}. We note that an early occurrence of primary peak times in surface topology is generally associated with increased drying heterogeneity.

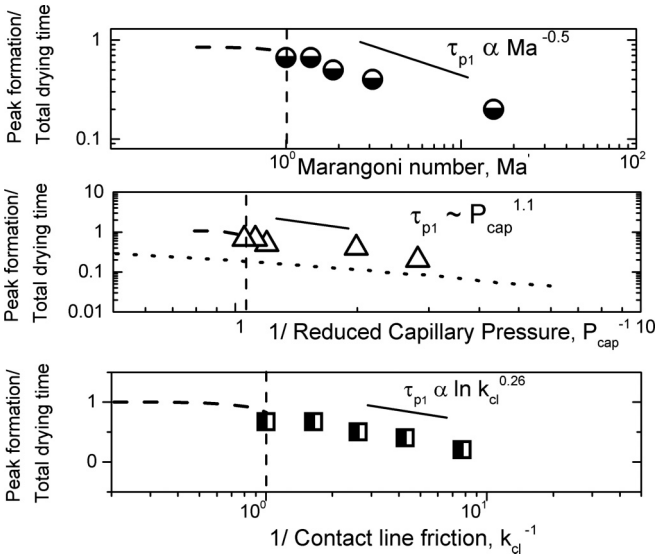

FIG. 9. Factors affecting fluid-line recession and onset of lateral drying heterogeneity. Experimental dependence of the dimensionless primary peak time τ_{P1}/τ_F on scaled Marangoni number Ma′, reduced capillary pressure P_{cap}, and contact-line friction k_{cl}. The dashed line represents the dilute limit data where no drying heterogeneity and thus no peak is observed before final drying of the film; in this regime, $\tau_{P1}/\tau_F \approx 1$. The vertical dashed line in all panels shows the transition from fluid-line pinning to fluid-line recession. The dotted line in the middle panel shows results from simulations based on the Routh-Russel model [11,12]. A detailed comparison of data and simulation results can be found in Fig. S8 in [21].

D. Capillary pressure and pressure drop in a packed bed

In our experiments, particle packing occurs at the edge of drops during the drying process, which directly impacts the dynamics of the receding fluid line. The role of capillary pressure on the dynamics of a receding contact line was previously considered by Routh and Russel [11]. In this work, the authors considered uniform evaporation from a flat fluid interface and used the lubrication approximation to derive an expression for a dimensionless quantity called reduced capillary pressure that is used to describe the onset of fluid-line recession due to pressure drop in the packed bed. In particular, the fluid line recedes only when the pressure drop P^* in the packed particle region exceeds the maximum capillary pressure ($P_{\text{max}} = 10\gamma/a$, where a is particle radius) supported by the particle interstices near the drop edge. Routh and Russel developed an expression for a dimensionless quantity called reduced capillary pressure P_{cap}, defined as the ratio of pressure drop in the film P^* to the maximum capillary pressure P_{max},

$$P_{\text{cap}} = P_{\text{max}}/P^* = \frac{10\gamma H k_p}{a\eta \dot{E} l_c^2}, \tag{22}$$

where $\dot{E}$ is the rate of evaporation (here the rate of decrease in droplet height H), η is the solvent viscosity, a is the particle radius, l_c is the capillary length, and k_p is known as the permeability of the particle bed packing, which was calculated to be $k_p = 5.4 \times 10^{-17}$ m^2 for random close packing of latex particles at the drop edge [2]. For the drops studied in this work, $l_c \gg R$ (i.e., the spherical drop limit), so we calculate pressure drop using the drop radius R as the relevant length scale instead of capillary length l_c. For $P_{\text{cap}} < 1$, the fluid line is predicted to recede, as the pressure drop required for fluid flow through the packed bed (towards the drop outer edges) can no longer be sustained by the capillary pressure.

Reduced capillary pressure P_{cap} is plotted as a function of latex volume fraction for our samples in Fig. 8. Interestingly, for our experiments, we found that the permeability k_p for random close packing agrees well with the criteria for contact-line recession (P_{cap} near unity), which coincides with the onset of lateral heterogeneity. We further measured the recession time of the fluid line from the edge of the drop τ_{rec} from optical experiments. In Fig. S8 in [21], these data are plotted together with first peak times and previous experimental and simulation data on drying films [12]. Based on these data, we further plot the primary peak time τ_{P1} as a function of inverse capillary pressure $1/P_{\mathrm{cap}}$ resulting from an increase in our suspension volume fractions (Fig. 9, middle panel). Here the dotted line shows results from an iterative simulation based on the Routh-Russel model [11] performed for drying films [12]. Taken together, our results suggest that the Routh-Russel model tends to underestimate the rapid rise in fluid recession time observed for drop experiments, which can be rationalized by considering that the model does not account for additional driving forces such as Marangoni flows and contact-line friction, which are thought to play a dominant role in drops as compared to flat films [4,6]. In any event, our data reveal a nearly linear power-law dependence of the primary peak time as a function of P_{cap} such that $\tau_{P1}/\tau_F \propto P_{\mathrm{cap}}^{1.1}$. However, we state this relationship with caution given the relatively small number of experimental observations in the relevant range of P_{cap}.

E. Reduced contact-line friction

In drying latex suspensions, film formation by close-packed colloids at the contact line leads to a change in surface wetting properties from a hydrophilic to a hydrophobic dry film. From this perspective, we further studied the effect of surface properties on fluid-line friction at drop edge. Recently, Man and Doi [4] developed an analytical model to describe drying droplets for dynamic contact lines. Interestingly, the model predicts a smooth transition between ringlike and mountainlike patterns upon changing contact-line friction, which ultimately affects mobility. In this model, the minimum energy dissipation principle is used to derive the evolution of contact-line position and deposition profile as a function of time. Energy is dissipated due to contact-line motion over the substrate, which is quantitatively captured using a phenomenological parameter ξ_{cl} denoting an enhanced friction constant at the contact line. In this way, ξ_{cl} is assumed to originate from substrate wetting properties and substrate defects. In particular, a dimensionless contact-line friction k_{cl} is defined by

$$k_{\mathrm{cl}} = \xi_{\mathrm{cl}}/\xi_{\mathrm{hydro}} = \frac{\xi_{\mathrm{cl}}\theta}{3C\eta}, \tag{23}$$

where θ is contact angle, C is a numerical constant, and η is the viscosity at the contact line. In this way, k_{cl} represents the friction coefficient at the contact line ξ_{cl} relative to hydrodynamic friction for a wetting surface ξ_{hydro}. Using Eq. (23), we can determine the position of maximum deposit density or peak position r_p as a function of the drop radius R and the contact-line friction constant k_{cl}:

$$r_p/R = \left(\frac{k_{\mathrm{cl}}}{2k_{\mathrm{cl}}+1}\right)^{1/2(1+k_{\mathrm{cl}})}. \tag{24}$$

According to Eq. (24), it follows that the fluid line remains pinned such that $r_p/R \to 1$ when $k_{\mathrm{cl}} \gg 1$, which yields the classic coffee-ring pattern. On the other hand, mountainlike deposits ($r_p/R \to 0$) are recovered for $k_{\mathrm{cl}} \ll 1$. For intermediate-k_{cl} values, volcanolike patterns are predicted.

We fit this model to our experimental data based on surface profilometry measurements (Fig. S9 in [21]). Overall, the model provides good agreement with the peak positions from our experimental results. Here we treated the contact-line friction constant k_{cl} as an effective fitting parameter, which enabled determination of k_{cl} as a function of latex volume fraction (Fig. 8). These results suggest that contact-line friction decreases by approximately three orders of magnitude upon increasing the latex dispersion volume fraction by over four orders of magnitude. Strikingly, the results show a power-law decay for k_{cl} as a function of latex volume fraction ϕ such that $k_{\mathrm{cl}} \propto \phi^{-0.7}$. Here it is noteworthy that the contact-line friction constant does not exhibit two distinct regimes between

dilute and nondilute latex concentrations, which starkly contrasts the competing mechanisms of film formation including surface-tension-driven flows and capillary pressure driving forces, where the functional dependence on latex volume fraction ϕ is quantitatively different in the low- and high-concentration regimes. Finally, we can analyze the first peak formation time τ_{P1} in the context of a volume fraction-dependent contact-line friction (Fig. 9, lower panel). Interestingly, we find that the dimensionless contact-line friction k_{cl} shows an exponential dependence on peak time τ_{P1}, but only in the high-latex-volume-fraction regime. As contact-line friction decreases, peak time drops according to $\tau_{P1}/\tau_F \propto 0.26 \ln k_{\mathrm{cl}}$.

V. CONCLUSION

In this work we studied drying in film-forming latex suspensions as a function of dispersion volume fraction ranging from the ultradilute concentration regime ($\phi = 1.25 \times 10^{-5}$) to the concentrated regime ($\phi = 0.4$). In general, our results show that suspensions with higher latex content experience prolonged drying together with more heterogeneous lateral drying. For concentrated latex suspensions, the initial contact line remains pinned while the fluid line recedes, which ultimately gives rise to lateral heterogeneity in drying. Dry deposited films show a classic coffee-ring profile in the dilute regime, which transitions to volcanolike profiles profiles at higher latex concentrations. Dynamic contact angles monitored during drying show a striking nonmonotonic decay for concentrated suspensions with two characteristic peaks. An analytical model was developed to explain the nonmonotonic contact-angle decay. The model was used to compare experimental and calculated values of peak strain and we find good agreement between the model and our experiment. Concentration-dependent experimental results were interpreted using different analytical models that probe factors affecting fluid-line recession, including Marangoni flows, reduced capillary pressure, and contact-line friction in drying latex suspensions.

Considering the various analytical models, it is possible to compare all three factors affecting lateral drying heterogeneity in film-forming droplets (Fig. 9). As previously discussed, a decrease in primary peak time τ_{P1} generally corresponds to increased drying heterogeneity. Our results suggest that Marangoni flows due to active interfacial species generally play a weaker role in determining drying heterogeneity compared to contact-line friction in all concentration regimes. In the dilute regime, high values of Marangoni number ($\mathrm{Ma} \gg 1$, originating from excess surfactant concentration used for latex particle stabilization) prove to not be a sufficient condition to induce fluid-line recession. In the higher-concentration regime, the relative peak time τ_{P1}/τ_F (and hence drying heterogeneity) is at least an order of magnitude more sensitive to changes in capillary pressure and reduction in contact-line friction compared to changes in Marangoni flows. We note that our quantitative relationship with Marangoni number here is based on SLS surfactant used to stabilize latex particles and can possibly be affected by use of a different interfacially active species.

This work studied phenomena at the intersection of the drop-drying community and the film-formation community. In terms of drop-drying phenomena, our work shows that drops of film-forming latex suspensions exhibit a nonmonotonic contact angle during drying. Several interesting features are revealed. First, the contact line is pinned and the fluid line recedes due to high-concentration latex suspensions. Second, the contact angle shows an interesting nonmonotonic decay due to stress accumulation and recovery in the compacted region. Third, the drying heterogeneity is affected not by altering substrate chemistry or solvent chemistry, but rather by increasing latex concentration. Fourth, the transition from homogeneous to heterogeneous drying in the context of a pinned and a receding fluid line that leads to coffee-ring and volcanolike profiles, respectively, is continuous, such that a common physical framework can be used to describe the process. Our work is consistent with a theoretical investigation on this topic [4].

With regard to the film-formation community, our results also show several interesting phenomena. First, film-forming latexes affect not just the capillary pressure, but also the contact-line friction at the substrate interface. Contact-line friction depends on latex concentration and directly contributes to fluid-line recession and lateral drying heterogeneity. Second, the compacted region

of the film-forming latex suspension is often considered to be dry and hence elastic in its material response [22]. Our results show that the compacted region can be described as a viscoelastic solid during long-time evaporation events near the solidification time point. Moreover, our model was further used to estimate the transient material properties for the compacted region, which ultimately determine the coating properties. Third, we show that increasing latex concentration in aqueous suspensions increases drying time, albeit at the cost of increasing drying heterogeneity. These conclusions are important because attempts to minimize drying heterogeneity generally affect open time for paints or alter the compacted film properties using open-time-extension additives. These chemical modifiers may in turn affect the material properties, drying heterogeneity, and contact-line friction in an interlinked fashion.

In applications involving film-forming latex suspensions, common challenges involve overly rapid drying times and/or unwanted lateral drying heterogeneity in surface topology, both of which are highly undesirable processing characteristics. In general, our work suggests that increases in total drying time associated with increased latex concentrations are accompanied by increases in drying heterogeneity. This stands true even after accounting for varying water content in these dispersions of varying concentration. Based on these findings, our results suggest that an increase in latex concentration (alone) will not provide a useful strategy to combat issues associated with heterogeneities in drying fronts and surface topologies. Studies aimed at addressing alternative strategies to decrease lateral and vertical heterogeneity, thereby increasing open time during film formation, are left for the future. Moving forward, an analytical model describing the comparative role of all three factors affecting heterogeneity (and possibly the evaporation rate) together with the unique viscoelastic-dependent drying kinetics of concentrated film-forming suspensions would greatly benefit a full understanding and analysis of these systems.

ACKNOWLEDGMENTS

This work was supported by the The Dow Chemical Company through the University Partnership Initiative Program, Grant No. 226772AA. We thank John Halligan for synthesizing the latex particles. We are grateful to Jim Bohling, Ant Van Dyk, Lin Wang, and Keith Harris for useful discussions and the Frederick Seitz Materials Research Laboratory at the University of Illinois at Urbana-Champaign for instrumentation.

[1] J. L. Keddie, Film formation of latex, Mater. Sci. Eng: R: Reports **21**, 101 (1997).

[2] J. L. Keddie and A. F. Routh, *Fundamentals of Latex Film Formation* (Springer Netherlands, Dordrecht, 2010).

[3] T. Kajiya, W. Kobayashi, T. Okuzono, and M. Doi, Controlling the drying and film formation processes of polymer solution droplets with addition of small amount of surfactants, J. Phys. Chem. B **113**, 15460 (2009).

[4] X. Man and M. Doi, Ring to Mountain Transition in Deposition Pattern of Drying Droplets, Phys. Rev. Lett. **116**, 066101 (2016).

[5] H. Kim, F. Boulogne, E. Um, I. Jacobi, E. Button, and H. A. Stone, Controlled Uniform Coating from the Interplay of Marangoni Flows and Surface-Adsorbed Macromolecules, Phys. Rev. Lett. **116**, 124501 (2016).

[6] T. Kajiya, C. Monteux, T. Narita, F. Lequeux, and M. Doi, Contact-line recession leaving a macroscopic polymer film in the drying droplets of water-poly(N,N-dimethylacrylamide) (PDMA) solution, Langmuir **25**, 6934 (2009).

[7] K. Fukuda, T. Sekine, D. Kumaki, and S. Tokito, Profile control of inkjet printed silver electrodes and their application to organic transistors, ACS Appl. Mater. Interfaces **5**, 3916 (2013).

[8] J. Park and J. Moon, Control of colloidal particle deposit patterns within picoliter droplets ejected by ink-jet printing, Langmuir **22**, 3506 (2006).

[9] V. R. Gundabala, C.-H. Lei, K. Ouzineb, O. Dupont, J. L. Keddie, and A. F. Routh, Lateral surface nonuniformities in drying latex films, AIChE J. **54**, 3092 (2008).
[10] A. M. König, T. G. Weerakkody, J. L. Keddie, and D. Johannsmann, Heterogeneous drying of colloidal polymer films: Dependence on added salt, Langmuir **24**, 7580 (2008).
[11] A. F. Routh and W. B. Russel, Horizontal drying fronts during solvent evaporation from latex films, AIChE J. **44**, 2088 (1998).
[12] J. M. Salamanca, E. Ciampi, D. A. Faux, P. M. Glover, P. J. McDonald, A. F. Routh, A. C. I. A. Peters, R. Satguru, and J. L. Keddie, Lateral drying in thick films of waterborne colloidal particles, Langmuir **17**, 3202 (2001).
[13] A. F. Routh and W. B. Zimmerman, Distribution of particles during solvent evaporation from films, Chem. Eng. Sci. **59**, 2961 (2004).
[14] H. M. van der Kooij, G. T. van de Kerkhof, and J. Sprakel, A mechanistic view of drying suspension droplets, Soft Matter **12**, 2858 (2016).
[15] R. D. Deegan, O. Bakajin, T. F. Dupont, G. Huber, S. R. Nagel, and T. A. Witten, Capillary flow as the cause of ring stains from dried liquid drops, Nature (London) **389**, 827 (1997).
[16] Y. Cai and B.-m. Zhang Newby, Marangoni flow-induced self-assembly of hexagonal and stripelike nanoparticle patterns, J. Am. Chem. Soc. **130**, 6076 (2008).
[17] K. L. Maki and S. KumarFast evaporation of spreading droplets of colloidal suspensions, Langmuir **27**, 11347 (2011)
[18] T. Pham and S. Kumar, Drying droplets of colloidal suspensions on rough substrates, Langmuir **33**, 10061 (2017).
[19] N. Tsapis, E. R. Dufresne, S. S. Sinha, C. S. Riera, J. W. Hutchinson, L. Mahadevan, and D. A. Weitz, Onset of Buckling in Drying Droplets of Colloidal Suspensions, Phys. Rev. Lett. **94**, 018302 (2005).
[20] H. M. Vale and T. F. McKenna, Adsorption of sodium dodecyl sulfate and sodium dodecyl benzenesulfonate on poly(vinyl chloride) latexes, Colloids Surf. A **268**, 68 (2005).
[21] See Supplemental Material at http://link.aps.org/supplemental/10.1103/PhysRevFluids.2.114304 for figures and a table.
[22] A. M. König, E. Bourgeat-Lami, V. Mellon, K. von der Ehe, A. F. Routh, and D. Johannsmann, Dilational lateral stress in drying latex films, Langmuir **26**, 3815 (2010).
[23] R. G. Larson, *The Structure and Rheology of Complex Fluids* (Oxford University Press, New York, 1999).
[24] J. Freed-Brown, Evaporative deposition in receding drops, Soft Matter **10**, 9506 (2014).
[25] A. F. Routh and W. B. Russel, Deformation mechanisms during latex film formation: Experimental evidence, Ind. Eng. Chem. Res. **40**, 4302 (2001).
[26] V. Divry, A. Gromer, M. Nassar, C. Lambour, D. Collin, and Y. Holl, Drying mechanisms in plasticized latex films: Role of horizontal drying fronts, J. Phys. Chem. B **120**, 6791 (2016).
[27] T. Kajiya, D. Kaneko, and M. Doi, Dynamical visualization of "coffee stain phenomenon" in droplets of polymer solution via fluorescent microscopy, Langmuir **24**, 12369 (2008).